

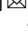

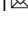







Light-matter interaction beyond Born-Oppenheimer approximation mediated by stimulated phonon polaritons

Yao Lu¹ , Qiang Wu¹  , Hao Xiong¹, Xu Zhou¹, Zhixuan Li¹, Jiwei Qi¹  , Xitan Xu¹ , Ruobin Ma¹, Jiang Fan¹, Zhigang Chen¹   & Jingjun Xu¹  

For decades, the light-matter interaction (LMI) based on Born-Oppenheimer (BO) approximation has dominated the fields of photonics, materials, and condensed-matter physics. However, in polar crystals, the BO approximation is not applicable when stimulated phonon polaritons are excited. Unlike the studies on topological physics and physical chemistry that go beyond BO approximation, here we unravel a stimulated phonon polariton-mediated LMI mechanism in polar crystals, which is radically different from the traditional LMI interpreted by BO approximation. In the regime of stimulated phonon polariton-mediated LMI, two exemplary experiments were conducted at different wavelengths: Q-factor increase of a LiNbO₃ terahertz microcavity, and a five orders-of-magnitude enhancement of second-harmonic generation of infrared laser pulses in a LiNbO₃ slab. Our study enhances the understanding of the LMI mechanism and shows potential for applications in the fields of optics/photonics and condensed-matter physics.

¹The Key Laboratory of Weak-Light Nonlinear Photonics, Ministry of Education, TEDA Applied Physics Institute and School of Physics, Nankai University, 300457 Tianjin, China. ✉email: wuqiang@nankai.edu.cn; qijw@nankai.edu.cn; zgchen@nankai.edu.cn; jjxu@nankai.edu.cn

Light-matter interaction (LMI) plays an indispensable role in optical physics¹. In the traditional LMI regime, electrons and ions are treated separately according to the Born–Oppenheimer (BO) approximation^{2,3}. Generally, electrons are considered to take the dominating role in the LMI processes, since ions are too heavy to respond to the fast electromagnetic oscillations of visible or near-infrared light. Therefore, the ionic contribution is typically ignored in most LMI processes, as illustrated in Fig. 1a. However, the ionic contribution plays an important role in many cases, such as Raman scattering or stimulated Raman scattering. Particularly, the ionic contribution is also unignorable in case that a low-frequency electromagnetic wave, such as a microwave or a terahertz (THz) wave, is inputting^{4–7}.

In polar crystals, the LMI process is inevitably affected by the stimulated phonon polaritons (SPhPs), which can be excited by the THz waves, as illustrated in Fig. 1b, c. In this case, the SPhPs dominate the LMI process, where the electronic states are modulated by the SPhP-excited ions, and therefore the visible/infrared light performs a different excitation. Therefore, the SPhPs render a distinctive mechanism of LMI which is fundamentally different from that of the traditional LMI which is mediated only by electrons, or by pure ions when the oscillation of the pump wave is far lower than that of the optical phonons without strong coupling⁷. Although the breakdown of BO approximation has been extensively explored in topological Berry phase, quantum chemistry, and molecular physics^{8–10}, most work on LMI in polar crystals is still based on BO approximation^{1–3}.

PhPs are a type of polaritons that are found in polar crystals. Recently, there emerged tremendous interests in long-wavelength light–matter interactions, from mid-infrared to THz polaritonics, in common optical crystals^{11–13}, where the novel effects have been revealed by the advanced experimental tools¹⁴. They originate from the coupling between optical phonons and radiated THz waves^{15–17}. Huang equations are sufficient to provide a good description for spontaneous PhPs (heat-excited), as verified by an example of measuring a GaP crystal in 1965^{15,16,18}. However, when polar crystals are excited by femtosecond laser pulses or THz waves, the SPhPs get generated and exhibit very different properties from that of spontaneous PhPs^{17,19–23}. Specifically, the SPhPs enable to achieve a giant nonlinearity or an efficient control over polar materials. Thus, we proposed nonlinear Huang equations to describe the nonlinearity of the SPhPs¹⁹.

Moreover, the SPhPs exhibit remarkable delocalization and coherence including both temporal coherence and spatial coherence¹⁹. This makes the BO approximation inapplicable. Here, the delocalization implies a high mobility of phonon polaritons, which could transport the ionic state quickly through the crystal but does not mean that the ions are moving through the lattice¹⁹. The SPhP-mediated LMI (SPhP-LMI) gives rise to a new mechanism that enables PhPs to be directly involved in the LMI and is a much more efficient mechanism than the traditional LMI mechanism. Furthermore, this mechanism makes significant changes to the ionic states directly and creates a significant impact on the electronic states through ion–electron coupling. This indicates promising prospects in the field of optical physics by covering a large range of wavelengths.

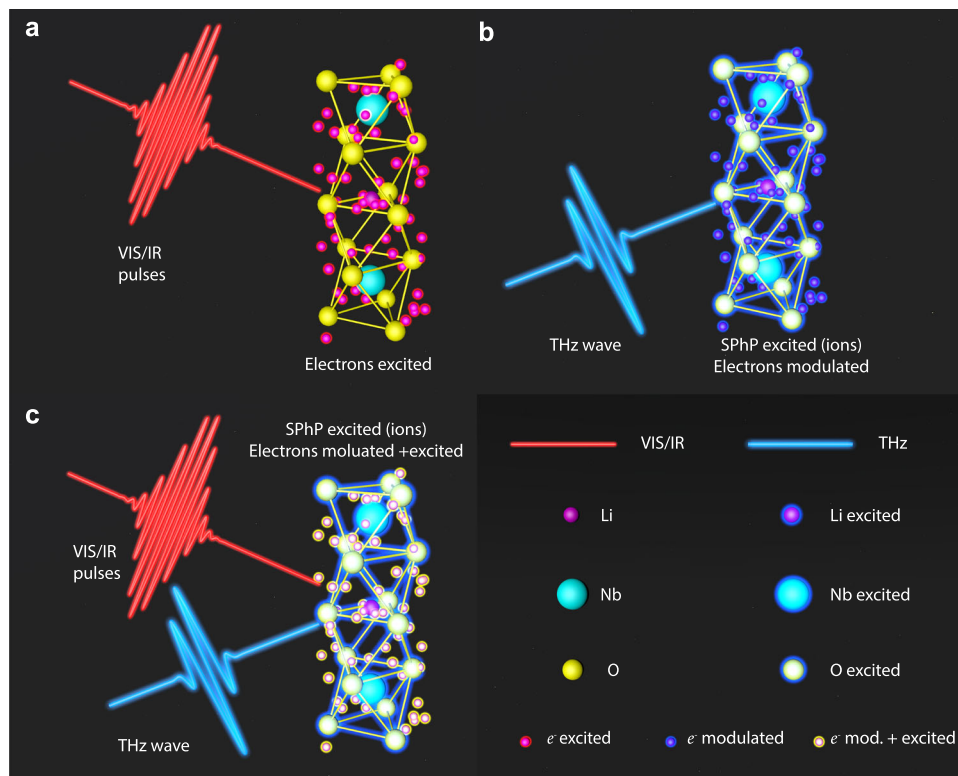


Fig. 1 Diagram of stimulated phonon polariton-mediated light–matter interaction (SPhP-LMI) in LiNbO₃ crystal. **a** Traditional LMI mechanism. Only electrons can be excited when visible/infrared light inputs the LiNbO₃ crystal, and the ions are hardly excited. **b** SPhP-LMI mechanism excited by THz waves. SPhPs are excited when THz waves input the LiNbO₃ crystal. The ions are modulated by SPhPs and show strong coherent delocalization, where electronic states are changed accordingly through ion–electron coupling. This indicates a distinct LMI between THz waves and LiNbO₃ crystal, beyond Born–Oppenheimer approximation. **c** SPhP-LMI mechanism excited by visible/infrared light with THz waves exciting SPhPs. Electronic states are thus modulated by the SPhP-induced coherently delocalized ions, so the visible/infrared light performs a different excitation, which results in a dramatical material modulation and finds a distinctive approach to achieving weak-light nonlinear photonics. Here Born–Oppenheimer approximation is not applicable.

In this study, we demonstrate the SPhP-LMI mechanism beyond BO approximation. The SPhP-LMI mechanism enables a series of phenomena for a large range of wavelengths and is experimentally demonstrated using LiNbO₃ polar crystals through two representative experiments: temporal evolution of THz waves in a microcavity and second-harmonic generation (SHG) of near-infrared laser pulses. The first experiment indicates that this mechanism can induce a significant loss reduction in the microcavity and thus increases its *Q* factor in the THz region. The second experiment demonstrates that the SPhP-LMI can enhance the SHG approximately 4.8×10^5 times for the near-infrared laser pulses. Moreover, we also discuss the rationality and general applicability of the SPhP-LMI in other closely related fields.

Results

SPhP-LMI mechanism in polar crystals. The SPhPs are usually generated when a polar crystal is pumped by external femtosecond laser pulses or THz waves. From a theoretical perspective, this process can be described by the nonlinear Huang equations^{19,24}, represented by Eq. (1)

$$\begin{aligned} \ddot{x} + \gamma \dot{x} + \omega_0^2 x &= (Nm)^{-1/2} bE - ax^2 + (q/m)E_{ex} \\ P &= (Nm)^{1/2} bx + \epsilon_0(\epsilon_\infty - 1)E, \end{aligned} \quad (1)$$

where x and ω_0 represent the motion amplitude and eigenfrequency of the ions, respectively, while γ and a represent their decay rate and the coefficient of the nonlinear restoring force, respectively. An external driving field E_{ex} acts on the ions whose effective mass and electrical charge are represented by m and q , respectively. N is the number of oscillators per unit volume. E and P indicate the macroscopic electric field and the polarization in the crystal, respectively. The coupling between phonons and the radiated THz waves is characterized by the constant $b = \omega_0 \sqrt{\epsilon_0(\epsilon_0 - \epsilon_\infty)}$, with ϵ_0 and ϵ_∞ representing the low- and high-frequency relative permittivity of the material, respectively. The permittivity of vacuum is $\epsilon_0 = 8.85 \times 10^{-12} \text{ F m}^{-1}$.

Different from the heat-excited spontaneous PhPs²⁵, the specialty of the SPhPs lies in the attendance of external coherent THz driving and the strong delocalization, which breaks the traditional LMI mechanism which is based on BO approximation. The traditional material model assumes that the ions are fixed in the crystal, where the electron-ion coupling is generally regarded as different energy band structure, so that only electrons can be directly excited by visible or infrared light, as illustrated in Fig. 1a. However, once THz waves are employed in the polar material, SPhPs are generated. They transport the ionic states by electromagnetic fields in the whole material, indicating a strong delocalization of the SPhPs and ionic states, which has been demonstrated in our previous work¹⁹. Furthermore, the external driving field makes the noncoherent ionic oscillations in spontaneous PhPs become coherent, which is guaranteed to confirm the external driving THz field and behaves in a regular temporal phase evolution. Moreover, the spatial coherence of the SPhPs is protected by the temporal coherence and strong delocalization. Therefore, THz waves can directly excite the ions of polar crystals via SPhP-LMI, as depicted in Fig. 1b. This results in a significant nonlinear LMI and induces a series of phenomena at the THz frequencies.

Moreover, the strong delocalization and the coherence of SPhPs change the electronic states and make it invalid to treat the ions and electrons separately. Here the electronic states are altered by SPhPs through ion-electron coupling. This in turn may lead to unexpected effects for high-frequency light, including both visible and infrared light, as illustrated in Fig. 1c. Two examples

were chosen to show the general applicability of the SPhP-LMI mechanism: one is a *Q* factor increase of LiNbO₃ microcavity at THz frequency, and the other is an SHG enhancement of near-infrared light pulses, from which we demonstrate that the SPhP-LMI mechanism is generally applicable at various wavelengths.

Q factor increase of a THz microcavity. To theoretically investigate this LMI mechanism in a THz microcavity, an ideal one-dimensional Fabry–Perot cavity was constructed and calculated by the finite-element method through COMSOL Multiphysics, where the cavity length $L = 200 \text{ } \mu\text{m}$ and the material absorption of the cavity loss are set by a complex refractive index of $n = 5.10 + 2.20 \times 10^{-2}i$, which is consistent with the LiNbO₃ crystal. The two boundaries are perfect electrical conductor layers with a reflectivity of 100%, as presented in Fig. 2a. A broadband THz source was placed in the middle of the cavity which radiates a Gaussian-form THz pulse with center frequency of 0.4 THz, duration of 2 ps (ranging from 0.2–0.6 THz in frequency), as shown in Fig. 2b.

When only Maxwell equations are used to solve the electromagnetic waves in the microcavity, the polarization field is determined by $P = \epsilon_0 \chi E$ with χ indicating the linear susceptibility. In this case, the electric field decays rapidly, as indicated by the red curves in Fig. 2c. However, when considering the SPhP-LMI mechanism, the coupled Maxwell equations and nonlinear Huang equations are solved in the microcavity, where the polarization field is determined by Eq. (1). Here, only the linear effect is considered, therefore the coefficient of the nonlinear restoring force a is set as zero. In this case, the electric field decays slowly, as indicated by the blue curve in Fig. 2c. This demonstrates a significant absorbance modulation through the SPhP-LMI mechanism in the microcavity. By taking a Fourier transformation, the spectral information of the confined THz waves in both cases is obtained as depicted in Fig. 2d. Accordingly, when considering the traditional optical microcavity, the *Q* factor is approximately 83.71, while this value is increased to 127.4 when the SPhP-LMI mechanism is involved, indicating a *Q* factor increase of approximately 52.2%.

In the experiment, an L3 photonic crystal microcavity is fabricated in an *x*-cut LiNbO₃ wafer (indicated by y direction in our experimental system), with a size of 1 mm (x) \times 0.05 mm (y) \times 1.1 mm (z), using the femtosecond laser direct writing technique (see Method)^{26,27}, where the lattice constant $a = 170 \text{ } \mu\text{m}$, unit radius $r = 50 \text{ } \mu\text{m}$, and shift $s = 0.15r$. After the microcavity is prepared, a femtosecond laser pulse is line-focused in the middle of the microcavity to generate THz PhPs, as illustrated in Fig. 3a. Since the LiNbO₃ microcavity slab is only 50 μm -thick, the generated THz PhPs propagate along the direction of *x*-axis^{21,28}. The L3 microcavity was laid vertically to ensure that only one mode of the microcavity can be excited. To acquire the spatio-temporal information regarding the THz PhPs, the pump-probe technique and phase-contrast imaging were employed (see Method and Supplementary Fig. 1)^{21,28–31}.

Figure 3b presents the temporal evolution of the THz PhPs in the microcavity (see Supplementary Movie 1). One can see that after THz PhPs are generated, they propagate bidirectionally along the *x*-axis. At approximately 2 ps, they reach the boundaries of the microcavity, and then the reflected PhPs unavoidably interfere with incident PhPs at 4 ps. At the same time, some energy leaks from the cavity. During this process, only the PhPs that match the cavity modes are allowed to be preserved, while others decay very quickly during the interference.

An energy band diagram for the photonic crystal is calculated and presented in Fig. 4a, in which a bandgap from 0.375 THz to 0.490 THz can be seen, and is marked by the gray region. By

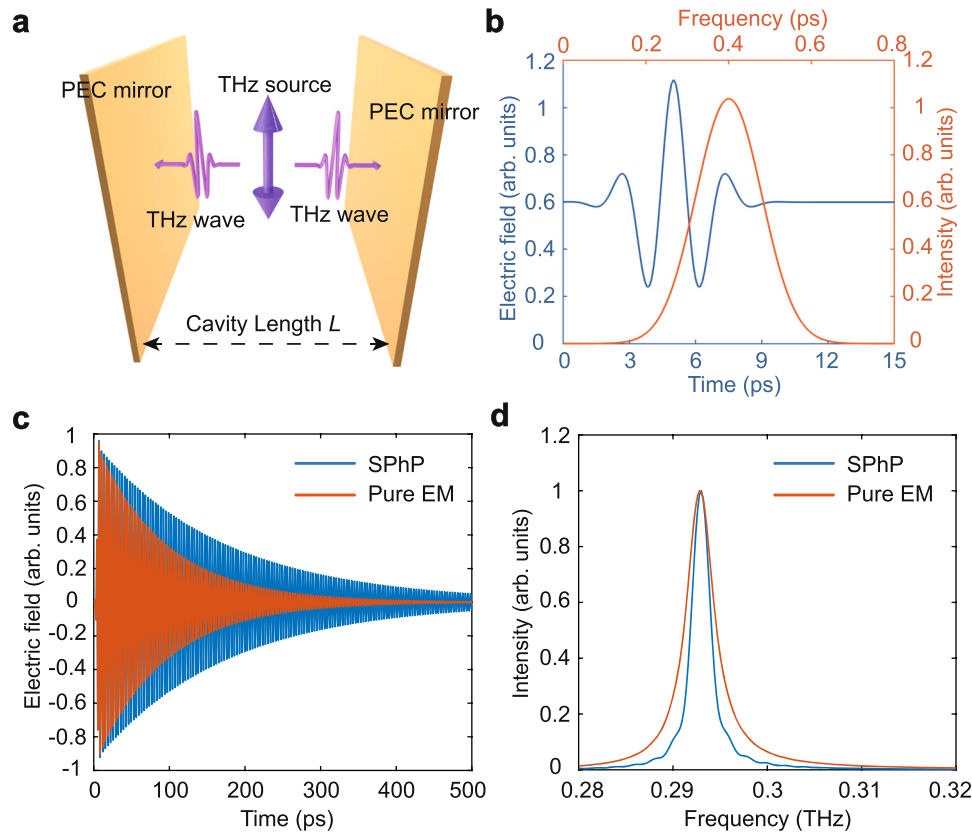


Fig. 2 Stimulated phonon polariton-mediated light-matter interaction in an ideal one-dimensional Fabry-Perot microcavity. **a** Diagram of the ideal Fabry-Perot microcavity with cavity length $L = 200 \mu\text{m}$. An absorption medium is placed between two perfect electrical conductor boundaries. A broadband THz source is placed in the middle of the microcavity. PEC: perfect electrical conductor. **b** Temporal trace and spectrum of the source emitted THz wave. **c** Decay of the electric field in the microcavity with and without considering the stimulated phonon polaritons. **d** The Fourier spectra of **c**.

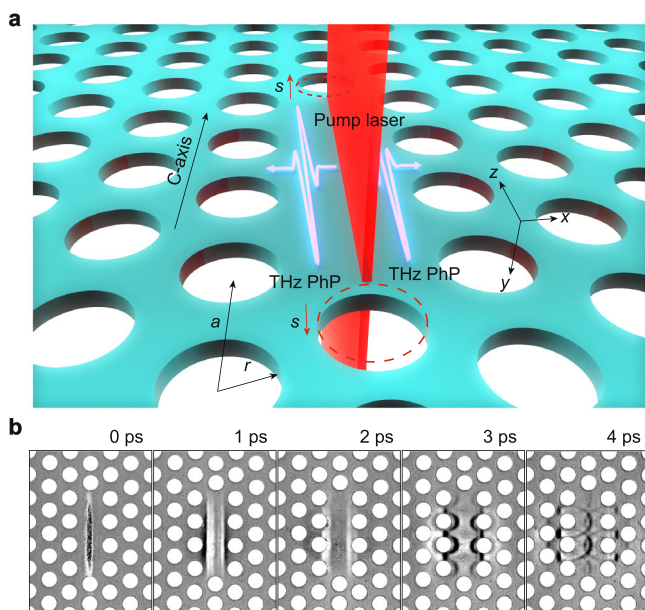


Fig. 3 Experimental design of the microcavity and measured temporal evolution of the THz phonon polaritons. **a** Illustration of the pump laser and layout of the microcavity. Parameters: $a = 170 \mu\text{m}$, $r = 50 \mu\text{m}$, $s = 0.15r$. **b** Temporal evolution of THz phonon polaritons in the microcavity. From left to right, are snapshots of the electric field of the THz phonon polaritons in the sample from $t = 0 \text{ ps}$ to 4 ps upon generation.

choosing a specific point, indicated by the black dot in the top inset of Fig. 4b, in the experimental results, we can obtain the decay of the electric field in the microcavity, as presented in Fig. 4b. In the bottom inset of Fig. 4b, the initial broadband oscillation is obtained by selecting the initial oscillation after the first 5 ps from the microcavity confined PhPs. Accordingly, the resonant mode can be easily identified from the Fourier spectra of the electric fields in the cavity and the broadband radiations, presented in Fig. 4c. The Q factor in the experiment was measured and found to be 68.83. Figure 4d presents the distribution of the electric field at the line indicated in the inset of Fig. 4d in the frequency domain.

Since we cannot remove the contribution of the SPhP-LMI in experiments, a finite-difference time-domain simulation was performed and employed as a reference case of pure electromagnetic waves without this mechanism. To ensure consistency, the geometry of the microcavity in the simulation was made to remain identical to the experiment. LiNbO_3 is regarded as a dielectric by ignoring its thermal influence, and its complex refractive index at 0.4 THz was set as $n_e = 5.10 + 2.20 \times 10^{-2}i$ for the extraordinary light which agrees well with the value in the experiment (see Supplementary Note 1).

The simulation results are presented in Fig. 4e, where the simulated microcavities have a resonant frequency of 0.421 THz . However, the Q factor of the simulated pure electromagnetic-wave microcavity is only 46.78, which is less than the value of 68.83, measured in the experiment mediated by the SPhP-LMI mechanism. Therefore, at least a 47.1% Q factor increase is attributed to the loss modulation induced by the SPhP-LMI

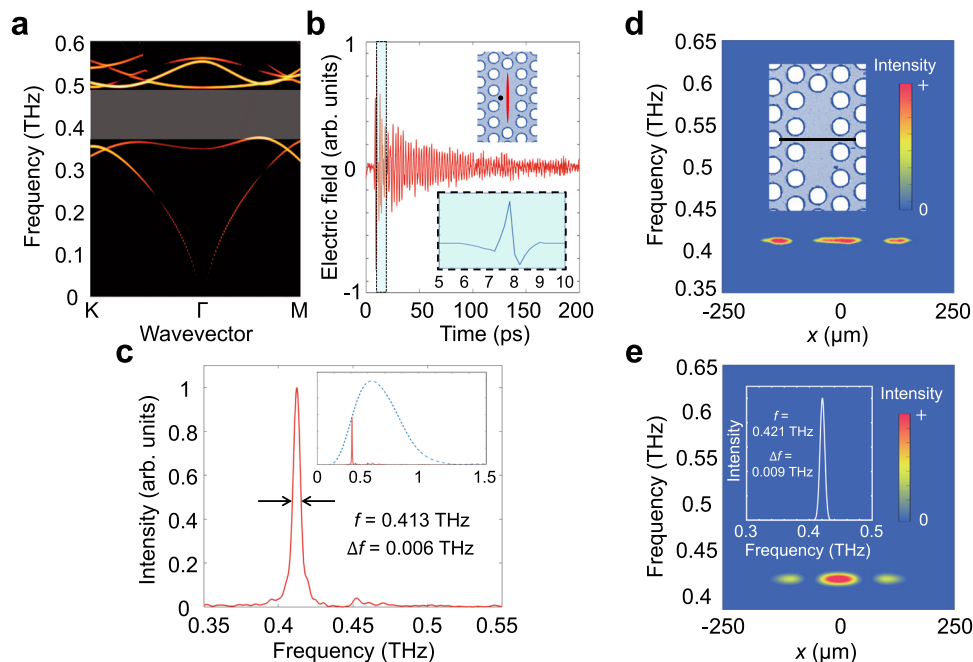


Fig. 4 Experimental phonon polaritons and simulated electromagnetic waves in the microcavity. **a** Energy bands of the LiNbO₃ photonic crystal. The gray region indicates the bandgap spanning from 0.375 to 0.490 THz in the band structure. **b** Electric field oscillation of a point in the microcavity, and the point is presented by the black dot in the top inset. The top inset also shows the pump position, while the bottom inset indicates the femtosecond laser-generated broadband THz phonon polaritons, the initial oscillation after the first 5 ps from the microcavity confined phonon polaritons. **c** Spectral information of the microcavity confined phonon polaritons, Fourier transformation of (**b**). The inset presents the spectral comparison between the broadband and localized phonon polaritons. **d** Simulated spectral information at the line shown by the inset, in the microcavity. **e** Spectral information along a line and at a point in the microcavity, where the positions of the line and the point are the same as in the experiment.

mechanism. This result indicates a good agreement with our expectations and presents the calculation of the ideal 1D Fabry–Perot microcavity. Besides, the *Q* factor is also influenced by the photonics design of the microcavity²⁶, and a thinner slab results in a larger *Q* value and a higher resonant frequency (see Supplementary Note 2).

SHG enhancement of near-infrared light pulses. After SPhPs are generated in a polar crystal, the ionic nonlinearity was greatly enhanced with the help of the SPhP-LMI mechanism, and thus the giant nonlinearity of THz waves was achieved¹⁹. Simultaneously, the electronic nonlinearity also gets increased because of the ion–electron coupling.

To verify this point, we examined the influence of the SPhP-LMI on near-infrared laser pulses. As illustrated in Fig. 5a, the femtosecond laser pulses were focused to generate an SHG signal in a LiNbO₃ crystal. The tilt-pulse setting was employed to distinguish the contributions of laser power and SPhPs^{19,22}. The first-order diffraction light of a 1200 mm^{−1} grating was focused by a 5 cm convex lens, and the LiNbO₃ crystal was moved from the image plane to the focus plane of the grating (see Supplementary Note 3). During this process, the SHG signal was recorded by a spectrometer at each position as presented in Fig. 5a.

According to the phase-match condition of the tilt-pulse settings, the SPhPs can only be excited if the LiNbO₃ crystal is placed at the image plane of grating²². Therefore, a strong SHG signal should be measured when the sample reaches this position. After that, although the sample moves closer to the focus plane and the power density of the laser pulses increases, the SHG signal should decrease as illustrated in Fig. 5a. The experimental observations well agree with this expectation. Figure 5b presents the SHG spectrum during the movement of the sample, and one

can see two local maximum values, each located in the focus and the image plane of the grating. According to the theoretical evaluation, the nonlinear susceptibility at the image plane which is enhanced by SPhP-LMI is approximately 4.8×10^5 times larger than the one at the focus plane (see Supplementary Note 3). The maximum value at the image plane is attributed to the SPhP-LMI mechanism, while the one at the focus plane is caused by the intense pump power, where the LiNbO₃ crystal is ablated soon at the focus plane. The peak intensity and the total average energy of the SHG signal depend on the position of the LiNbO₃ sample as presented in Fig. 5c.

Generally, the microscopic polarization of materials includes dipolar polarization (orientation), ionic polarization, and electronic polarization (including distortion of electron cloud). While for ionic crystals of LiNbO₃, ionic polarization and electronic polarization both contribute to the nonlinear polarizations. Generally, where there are no SPhPs, the ionic polarization is less possible to be directly excited by visible or infrared light since the ions are too heavy to respond such fast oscillations are ignored. However, the potential energy between ions are determined by Madelung constant, and its form is highly enharmonic so as to generate optical nonlinearity.

Nevertheless, electronic polarization, the one that can only be excited by visible or infrared light, is much weaker, which acquires most nonlinearity by electron–ions coupling. Therefore, the optical nonlinearity in the traditional case is very low excited only by polarizing electrons.

After SPhPs join in this process, the LMI process is changed. The spontaneous PhP originates the coupling of radiated THz waves (photons) by lattice vibration and phonons, while the SPhPs (stimulated) is a much stronger version excited by input THz waves. Thus, the ionic nonlinearity is utmost activated through the mechanism of “input THz waves → lattice

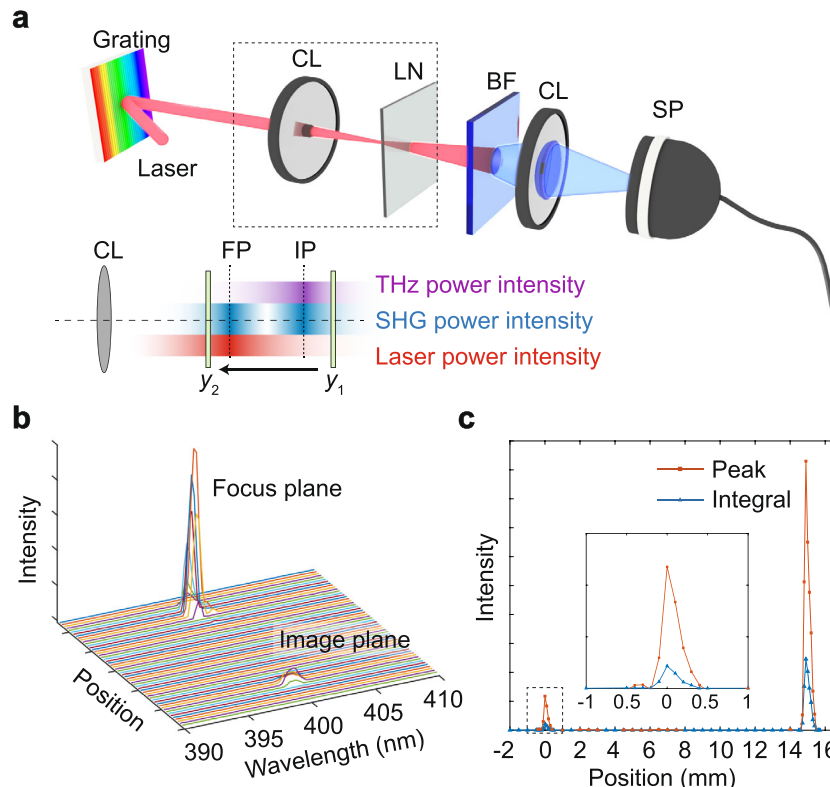


Fig. 5 Second-harmonic generation (SHG) enhancement of near-infrared laser pulses due to the stimulated phonon polariton-mediated light-matter interaction. **a** Experimental setup for excitation of the stimulated phonon polaritons and the measurement of SHG signal of infrared laser pulses. CL: convex lens; LN: lithium niobate slab; BF: blue filter; SP: spectrometer; FP: focus plane; IP: image plane. **b** Spectra of the SHG signal obtained by moving the LN slab. **c** Peak intensity and the total energy of the SHG signal when the sample is moved. The inset shows the details of the peak value near the image plane.

vibrations \longleftrightarrow radiated THz waves". Accordingly, the electronic nonlinearity is enhanced so that the tremendously SHG enhancement is observed.

Discussion

In the above experiments, the influences of the SPhP-LMI on the absorption of THz microcavity and the efficiency of near-infrared laser SHG were studied. Furthermore, the significance of the SPhP-LMI can extend to other fields where many expected effects can be found by experimental evidence in the literature results. However, the contribution of SPhP has not yet been paid enough attention.

THz-induced nonlinearity is one of the most important results and mainly includes two types of discoveries. The first one is by using THz waves to break the centrosymmetric properties of the materials and for generating even-order nonlinearities in materials such as THz-induced SHG^{31,32}. Generally, the centrosymmetric materials cannot support the generation of even-order nonlinear phenomena. Later, researchers found that THz waves can be used to induce SHG in centrosymmetric materials because they can excite SPhPs so as to break the symmetrical property of these materials^{31,32}. The second one is using THz waves to enhance the nonlinearity by exciting SPhPs. The most direct result of the SPhP-LMI is to achieve giant THz nonlinearities by tremendously increasing the ionic nonlinearity^{19,32–34}. Besides, the SPhPs change the electronic nonlinearity by "ion-electron" coupling so that the nonlinear polarization of high-frequency light such as SHG, Kerr effect, and Pockels effect can be improved^{21,35–37}. Especially, the Pockels effect which is generally used to detect THz waves²¹.

THz-induced spin and magnetism is another well-debated topic^{38–42}. The magnetism of the materials always depends on the spin of certain ions, such as iron or nickel, whereas the magnetization and demagnetization of the materials can be modulated by controlling the ionic spin of such materials. Generally, the magnitude of the macroscopic magnetization field is determined by both the external magnetic field and the restraint of the lattice. After the SPhPs get generated, the delocalization property of the PhPs would ease this restraint and significantly amplify the magnetization. The electric polarization can be improved in polar crystals in a similar way so that THz waves can be used to induce ferroelectricity since the restraint can be eased by SPhPs. The pertinent result was demonstrated in 2019⁴³.

Moreover, some experiments also demonstrated that THz waves can induce phase transitions including topological phase transition and Mott phase transition (insulator to metal transition)^{43–46}. THz waves can also induce the Stark effect and thermal effect, and drive ionic flow in a superionic conductor^{46–49}. All of these ion-dependent properties can be induced or modulated through the SPhP-LMI mechanism in polar crystals.

Conclusions

In conclusion, we demonstrated the SPhP-LMI mechanism in polar crystals. This mechanism dominates the LMI processes when THz waves are involved and the Born–Oppenheimer approximation is broken. With the attendance of the SPhPs, nonlinear LMI can be easily achieved so as to alter the optical properties of the polar crystals (abundant materials in nature). The strong delocalization and coherence of SPhPs break the Born–Oppenheimer approximation so that the ions and electrons

in the LMI can no longer be treated separately. Furthermore, the electronic states are modulated accordingly, indicating a remarkable nonlinear LMI phenomenon. We use two typical examples in LiNbO₃ polar crystals to experimentally demonstrate this mechanism at various wavelengths: Q factor enhancement of a LiNbO₃ terahertz microcavity and the giant SHG enhancement of near-infrared laser pulses. In the THz microcavity, the nonlinear mechanism led to an increase of the Q factor cavity by more than 50%, illustrating a completely different approach. On the other hand, this mechanism indeed led to an increase of five orders of magnitude in the SHG signals of near-infrared laser pulses.

This study proposes a distinctive LMI mechanism in polar crystals, which introduces extra possibilities that do not rely on the traditional LMI mechanism within the BO approximation. For instance, this mechanism enables more effective modulations of the optical properties and domain structures of the polar crystals by directly controlling ions, this breaks the restrictions of the very limited modulation by merely controlling electrons. Our findings are not only important for the development of optical and photonic devices but may also prove relevant for the understanding of other polariton-based phenomena in condensed-matter physics.

Methods

Fabrication of the LN photonic crystal. We use the femtosecond (fs) laser direct writing technique to fabricate the microcavity structure used in our experiment²⁷. About 2 μm protective coatings (SiO₂) are deposited on both surfaces of the LiNbO₃ slab. Subsequently, 5 μJ fs-laser pulses (amplified Ti:sapphire laser pulses, 800 nm central wavelength, 120 fs duration, 1 kHz repetition rate) are focused with a 0.25 NA objective to a spot size of approximately 4 μm and then used to mill the microcavity. A three-dimensional translation stage holds the 50 μm thick LiNbO₃ slab and is programmed to move laterally such that the outline of a circle is irradiated and drilled through the depth of the slab. Repeated operations of this sort are used to carve a series of periodic structures. After machining, the SiO₂ layers are removed with a hydrofluoric acid solution, which also removes any LiNbO₃ debris that is ejected during the machining process. These steps guarantee an optical-quality surface.

Generation and probing of the THz PhPs. The experiments are carried out using a Ti:sapphire fs-laser system with a central wavelength of 800 nm, a repetition rate of 1 kHz, and a pulse duration of about 120 fs. As shown in Supplementary Fig. 1, the laser output is split into a pump-pulse (400 μJ) and a probe-pulse (frequency-doubled, 400 nm, 50 μJ), which can be delayed relative to one another.

The pump pulse is directed to a mechanical time-delay line, and then line-focused into the center of the microcavity by a cylindrical lens with a focal length of 15 cm. After the pump pulses enter the sample, the THz PhPs are generated by a nonlinear optical process. Due to the polarization of the pump pulse being chosen parallel with the optical axis of the sample (z-direction), the generated THz pulses mainly propagate as the transverse electric modes of the slab microcavity. Here, the time-dependent information is obtained by adjusting the time delay of the pump pulse.

The generated THz PhPs propagate along the x-direction in the microcavity²¹. In order to visualize this field, a probe beam is employed that is spatially filtered and expanded to homogeneously illuminate the entire sample. This beam propagates in the y-direction through the sample of thickness *l* and thereby gathers an integral phase shift of $\Delta\phi_{\text{probe}}(x, z)$. Because the refractive index of the LiNbO₃ at a THz frequency is higher, it propagates slower than the probe beam. Thus, this integral phase-shift maps approximately the effective projection $E_{\text{THz}}(x, z)$ of the electric field of the THz PhPs along the beam path, i.e., it is more or less the integral of the electric field along the beam path. The relation between this projection field $E_{\text{THz}}(x, z)$ and the phase shift is given by the following equation:

$$\Delta\phi_{\text{probe}}(x, z) = 2\pi \frac{l}{\lambda_{\text{probe}}} \Delta n(x, z) = 2\pi \frac{l}{\lambda_{\text{probe}}} \frac{n_e^3 r_{33}}{2} E_{\text{THz}}(x, z), \quad (2)$$

where *l* is the thickness of the sample and λ_{probe} is the wavelength of the probe beam. The extraordinary polarization is chosen for all the electromagnetic fields, i.e., the pump, probe, and the THz waves, to achieve an optimum signal for the LiNbO₃ crystal under investigation. Accordingly, n_e and r_{33} denote in Eq. (2) the (extraordinary) refractive index and the electro-optic coefficient of the LiNbO₃ crystal, respectively.

To make the phase-shift visible, a phase-contrast imaging technique is employed: it consists of a CCD camera together with a 4f system (with

two achromatic lenses each having a focal length of 10 cm) and a phase plate in the Fourier plane of the system. The phase plate introduces a $\lambda/4$ phase shift to the zero-order diffraction component in the Fourier plane. Thus, the phase image was transformed into an intensity image according to the equation²¹:

$$I(x, z) = I_0(x, z) \left\{ 3 - 2 \left[\cos \Delta\phi_{\text{probe}}(x, z) - \sin \Delta\phi_{\text{probe}}(x, z) \right] \right\} \approx I_0(x, z) \left[1 + 2 \Delta\phi_{\text{probe}}(x, z) \right] \quad (3)$$

where $I_0(x, z)$ is the intensity distribution of the original probe beam ($\Delta\phi_{\text{probe}} = 0$). The phase in the sample is retrieved from:

$$\Delta\phi_{\text{probe}}(x, z) \approx \frac{1}{2} \left[\frac{I(x, z)}{I_0(x, z)} - 1 \right] = \frac{1}{2} \frac{\Delta I(x, z)}{I_0(x, z)} \quad (4)$$

with $\Delta I = I - I_0$.

Data availability

Supplementary Information and Supplementary Movie 1 are available for this paper.

Correspondence and requests for materials should be addressed to Y.L.

(yaolu@nankai.edu.cn) or Q.W. (wuqiang@nankai.edu.cn).

Received: 10 May 2022; Accepted: 8 November 2022;

Published online: 23 November 2022

References

- Weiner, J., Ho, P. T. & Dee, K. C. *Light-Matter Interaction: Fundamentals and Applications* Vol. 1 (Wiley, 2002).
- Born, M. & Oppenheimer, J. R. Zur quantentheorie der molekeln. *Ann. Phys.* **84**, 457 (1927).
- Ziman, J. M. *Electrons and Phonons: The Theory of Transport Phenomena in Solids* (Oxford University Press, 2001).
- Nicoletti, D. & Cavalleri, A. Nonlinear light-matter interaction at terahertz frequencies. *Adv. Opt. Photonics* **8**, 401 (2016).
- Mitrano, M. et al. Possible light-induced superconductivity in K₃C₆₀ at high temperature. *Nature* **530**, 461 (2016).
- Mayer, A. & Keilmann, F. Far-infrared nonlinear optics. I. $\chi^{(2)}$ near ionic resonance. *Phys. Rev. B* **33**, 6954 (1986).
- Boyd, G. D., Bridges, T. J., Pollack, M. A. & Turner, E. H. Microwave nonlinear susceptibilities due to electronic and ionic anharmonicities in acentric crystals. *Phys. Rev. Lett.* **26**, 387 (1974).
- Baer, M. *Beyond Born-Oppenheimer: Electronic Nonadiabatic Coupling Terms and Conical Intersections* (John Wiley & Sons, 2006).
- Butler, L. J. Chemical reaction dynamics beyond the Born-Oppenheimer approximation. *Annu. Rev. Phys. Chem.* **49**, 125 (1998).
- Mukherjee, B. Beyond Born-Oppenheimer theory for spectroscopic and scattering processes. *Int. Rev. Phys. Chem.* **38**, 287 (2019).
- Zhang, Q. et al. Interface nano-optics with van der Waals polaritons. *Nature* **597**, 187 (2021).
- Ma, W. et al. Ghost hyperbolic surface polaritons in bulk anisotropic crystals. *Nature* **596**, 362 (2021).
- Passler, N. C. et al. Hyperbolic shear polaritons in low-symmetry crystals. *Nature* **602**, 595 (2022).
- Cocker, T. L., Jelic, V., Hillenbrand, R. & Hegmann, F. A. Nanoscale terahertz scanning probe microscopy. *Nat. Photonics* **15**, 558 (2021).
- Huang, K. Lattice vibrations and optical waves in ionic crystals. *Nature* **167**, 779 (1951).
- Huang, K. On the interaction between the radiation field and ionic crystals. *Proc. R. Soc. A* **208**, 352 (1951).
- Feurer, T., Stoyanov, N. S., Ward, D. W., Vaughan, J. C. & Nelson, K. A. Terahertz polaritonics. *Annu. Rev. Mater. Res.* **37**, 317 (2007).
- Henry, C. H. & Hopfield, J. J. Raman scattering by polaritons. *Phys. Rev. Lett.* **15**, 964 (1965).
- Lu, Y. et al. Giant enhancement of THz-frequency optical nonlinearity by phonon polariton in ionic crystals. *Nat. Commun.* **12**, 3183 (2021).
- Dougherty, T. P., Wiederrecht, G. P., Nelson, K. A., Garrett, M. H. & Warde, C. Femtosecond resolution of soft mode dynamics in structural phase transitions. *Science* **258**, 770 (1992).
- Wu, Q. et al. Quantitative phase contrast imaging of THz electric fields in a dielectric waveguide. *Opt. Express* **17**, 9219 (2009).
- Lin, K. H., Werley, C. A. & Nelson, K. A. Generation of multicycle terahertz phonon polariton waves in a planar waveguide by tilted optical pulse fronts. *Appl. Phys. Lett.* **95**, 103304 (2009).

23. Auston, D. H., Cheung, K. P., Valdmanis, J. A. & Kleinman, D. A. Cherenkov radiation from femtosecond optical pulses in electro-optic media. *Phys. Rev. Lett.* **53**, 1555 (1984).
24. Lu, Y., Wu, Q., Xiong, H., Chen, Z. & Xu, J. Giant nonlinearity of THz waves mediated by photon-phonon strong coupling. In: *Conference on Lasers and Electro-Optics* (Optica Publishing Group, 2020) FF2Q.2.
25. Born, M. & Huang, K. *Dynamical Theory of Crystal Lattices* (Oxford University Press, 1954).
26. Akahane, Y., Asano, T., Song, B. S. & Noda, S. High-Q photonic nanocavity in a two-dimensional photonic crystal. *Nature* **425**, 944 (2003).
27. Sivarajah, P., Werley, C. A., Ofori-Okai, B. K. & Nelson, K. A. Chemically assisted femtosecond laser machining for applications in LiNbO₃ and LiTaO₃. *Appl. Phys. A* **112**, 615 (2013).
28. Peier, P., Pilz, S., Müller, F., Nelson, K. A. & Feurer, T. Analysis of phase contrast imaging of terahertz phonon-polaritons. *J. Opt. Soc. Am. B* **25**, B70 (2008).
29. Lu, Y. et al. Time-resolved imaging of mode-conversion process of terahertz transients in subwavelength waveguides. *Front. Phys.* **14**, 42502 (2019).
30. Yang, C., Wu, Q., Xu, J., Nelson, K. A. & Werley, C. A. Experimental and theoretical analysis of THz-frequency, direction-dependent, phonon polariton modes in a subwavelength, anisotropic slab waveguide. *Opt. Express* **18**, 26351 (2010).
31. Chen, J., Han, P. & Zhang, X. C. Terahertz-field-induced second-harmonic generation in a beta barium borate crystal and its application in terahertz detection. *Appl. Phys. Lett.* **95**, 011118 (2009).
32. Cornet, M., Degert, J., Abraham, E. & Freysz, E. Terahertz-field-induced second harmonic generation through Pockels effect in zinc telluride crystal. *Opt. Lett.* **39**, 5921 (2014).
33. Kozina, M., Fechner, M., Marsik, P., van, Driel, T. & Terahertz-driven, J. phonon upconversion in SrTiO₃. *Nat. Phys.* **15**, 387 (2019).
34. Fan, K., Hwang, H. Y., Liu, M., Strikwerda, A. C. & Averitt, R. D. Nonlinear terahertz metamaterials via field-enhanced carrier dynamics in GaAs. *Phys. Rev. Lett.* **110**, 217404 (2013).
35. Hirori, H. & Tanaka, K. Nonlinear optical phenomena induced by intense single-cycle terahertz pulses. *IEEE J. Sel. Top. Quantum Electron.* **19**, 8401110 (2013).
36. Vicario, C., Shalaby, M. & Hauri, C. P. Subcycle extreme nonlinearities in gap induced by an ultrastrong terahertz field. *Phys. Rev. Lett.* **118**, 083901 (2017).
37. Zalkovskij, M., Strikwerda, A. C., Iwaszczuk, K. & Popescu, A. Terahertz-induced Kerr effect in amorphous chalcogenide glasses. *Appl. Phys. Lett.* **103**, 221102 (2013).
38. Baierl, S. et al. Nonlinear spin control by terahertz-driven anisotropy fields. *Nat. Photonics* **10**, 715 (2016).
39. Baierl, S. et al. Terahertz-driven nonlinear spin response of antiferromagnetic nickel oxide. *Phys. Rev. Lett.* **117**, 197201 (2016).
40. Reid, A., Rasing, T., Pisarev, R. V., Duerr, H. A. & Hoffmann, M. C. Terahertz-driven magnetism dynamics in the orthoferrite DyFeO₃. *Appl. Phys. Lett.* **106**, 082403 (2015).
41. Bonetti, S. et al. THz-driven ultrafast spin-lattice scattering in amorphous metallic ferromagnets. *Phys. Rev. Lett.* **117**, 087205 (2016).
42. Shalaby, M., Vicario, C. & Hauri, C. P. Low frequency terahertz-induced demagnetization in ferromagnetic nickel. *Appl. Phys. Lett.* **108**, 182903 (2016).
43. Li, X. et al. Terahertz field induced ferroelectricity in quantum paraelectric SrTiO₃. *Science* **364**, 1079 (2019).
44. Liu, M. et al. Terahertz-field-induced insulator-to-metal transition in vanadium dioxide metamaterial. *Nature* **487**, 345 (2012).
45. Zhou, J., Xu, H., Shi, Y. & Li, J. Topological phase transition: terahertz driven reversible topological phase transition of monolayer transition metal dichalcogenides. *Adv. Sci.* **8**, 2003832 (2021).
46. Shu, M. J., Zalden, P., Chen, F., Weems, B. & Lindenberg, A. M. Ultrafast terahertz-induced response of GeSbTe phase-change materials. *Appl. Phys. Lett.* **104**, 251907 (2014).
47. Pein, B. C., Lee, C. K., Shi, L., Shi, J. J. & Nelson, K. A. Terahertz-driven Stark spectroscopy of CdSe and CdSe-CdS core-shell quantum dots. *Nano Lett.* **19**, 8125 (2019).
48. Minami, Y., Ofori-Okai, B. K., Sivarajah, P., Katayama, I. & Suemoto, T. Macroscopic ionic flow in a superionic conductor Na⁺ β-alumina driven by single-cycle terahertz pulses. *Phys. Rev. Lett.* **124**, 147401 (2020).
49. Pein, B. C. et al. Terahertz-driven luminescence and colossal Stark effect in CdSe-CdS colloidal quantum dots. *Nano Lett.* **124**, 5375 (2017).

Acknowledgements

This work is supported by the National Natural Science Foundation of China (11974192, 11874229, and 12134006), the Foundation of State Key Laboratory of Laser Interaction with Matter (SKLLIM2101), the 111 Project (B07013), and the Program for Changjiang Scholars and Innovative Research Team in University (IRT_13R29).

Author contributions

Q.W. and J.X. provided the basic idea, Y.L., Q.W., and J.Q. developed the concept, Y.L., H.X., and X.Z. implanted the experiment and carried out the data analysis with the help of Q.W. and Z.C., Y.L. wrote the paper, Z.L., X.X., R.M., and J.F. edited the paper, Q.W. and J.X. supervised the project.

Competing interests

The authors declare no competing interests.

Additional information

Supplementary information The online version contains supplementary material available at <https://doi.org/10.1038/s42005-022-01080-1>.

Correspondence and requests for materials should be addressed to Qiang Wu, Jiwei Qi, Zhigang Chen or Jingjun Xu.

Peer review information *Communications Physics* thanks Guangwei Hu and the other, anonymous, reviewer(s) for their contribution to the peer review of this work. Peer reviewer reports are available.

Reprints and permission information is available at <http://www.nature.com/reprints>

Publisher's note Springer Nature remains neutral with regard to jurisdictional claims in published maps and institutional affiliations.



Open Access This article is licensed under a Creative Commons Attribution 4.0 International License, which permits use, sharing, adaptation, distribution and reproduction in any medium or format, as long as you give appropriate credit to the original author(s) and the source, provide a link to the Creative Commons license, and indicate if changes were made. The images or other third party material in this article are included in the article's Creative Commons license, unless indicated otherwise in a credit line to the material. If material is not included in the article's Creative Commons license and your intended use is not permitted by statutory regulation or exceeds the permitted use, you will need to obtain permission directly from the copyright holder. To view a copy of this license, visit <http://creativecommons.org/licenses/by/4.0/>.

© The Author(s) 2022